FULL PAPER

# Internal Magnetic Structure of Nanoparticles Dominates Time-Dependent Relaxation Processes in a Magnetic Field

*Cindi L. Dennis,* Kathryn L. Krycka, Julie A. Borchers, Ryan D. Desautels, Johan van Lierop, Natalie F. Huls, Andrew J. Jackson, Cordula Gruettner, and Robert Ivkov**

Magnetic nanoparticles provide a unique combination of small size and responsiveness to magnetic fields making them attractive for applications in electronics, biology, and medicine. When exposed to alternating magnetic fields, magnetic nanoparticles can generate heat through loss power mechanisms that continue to challenge a complete physical description. The influence of internal nanoparticle (intracore) magnetic domain structure on relaxation remains unexplored. Within the context of potential biomedical applications, this study focuses on the dramatic differences observed among the specific loss power of three magnetic iron oxide nanoparticle constructs having comparable size and chemical composition. Analysis of polarization analyzed small angle neutron scattering data reveals unexpected and complex coupling among magnetic domains within the nanoparticle cores that influences their interactions with external magnetic fields. These results challenge the prevailing concepts in hyperthermia which limit consideration to size and shape of magnetic single domain nanoparticles.

## 1. Introduction

Magnetic nanostructured materials have garnered interest for over 100 years because their responsiveness to magnetic fields is important in science and technology.[1–6] Medical applications with biocompatible magnetic colloid suspensions now include ex vivo diagnostic tools,[7] and in vivo imaging[8,9] and therapy such as cancer hyperthermia,[10,11] and drug delivery.[12] For hyperthermia, choice of materials and structure are significantly constrained by biocompatibility, biodistribution, pharmacokinetics, toxicity, and clearance which define tolerable doses for the desired therapeutic benefits.[13–18] The magnetic properties of the nanoparticles, however, determine their functional capabilities; yet relatively little effort has been devoted to understand the magnetic forces operating within magnetic nanoparticles and the effects such micromagnetic structure exert on interactions with external magnetic fields.

Heat is a potent anticancer agent that also enhances radiation therapy by inhibiting DNA-damage repair.[19–22] Magnetic nanoparticles can deposit heat when they are exposed to time-varying or alternating magnetic fields (AMFs).[23,24] Therefore, the utility of magnetic nanoparticles for cancer hyperthermia has been recognized for over five decades,[25] but clinical application remains limited.[13] Insufficient thermal potency of nanoparticle preparations, which leads to ineffective therapy with clinically realistic nanoparticle and

Dr. C. L. Dennis, Dr. N. F. Huls
Material Measurement Laboratory, NIST
Gaithersburg, MD 20899-8552, USA
E-mail: cindi.dennis@nist.gov
Dr. K. L. Krycka, Dr. J. A. Borchers, Dr. A. J. Jackson,[+] Prof. R. Ivkov
NIST Center for Neutron Research
NIST, Gaithersburg, MD 20899-6102, USA
E-mail: rivkov1@jhmi.edu
R. D. Desautels, Prof. J. van Lierop
Department of Physics and Astronomy
University of Manitoba
Winnipeg, Manitoba R3T 2N2, Canada
Dr. A. J. Jackson
Department of Chemical Engineering
University of Delaware
Newark, DE 19716, USA
Dr. C. Gruettner
Micromod Partikeltechnologie, GmbH
18119 Rostock-Warnemuende, Germany

Prof. R. Ivkov
Department of Radiation Oncology and Molecular
Radiation Sciences
Johns Hopkins University School of Medicine
Baltimore, MD 21231, USA
Prof. R. Ivkov
Department of Oncology
Johns Hopkins University School of Medicine
Baltimore, MD 21231, USA
Prof. R. Ivkov
Institute for NanoBioTechnology
Johns Hopkins University
Baltimore, MD 21218, USA
Prof. R. Ivkov
Department of Materials Science and Engineering
Johns Hopkins University
Baltimore, MD 21218, USA
[+]Present address: European Spallation Source, 22100 Lund, Sweden

www.MaterialsViews.com

ADVANCED
FUNCTIONAL
MATERIALS
www.afm-journal.de

FULL PAPER

AMF combinations, remains a barrier for cancer hyperthermia. Stated another way—significant demand is placed upon a small quantity of nanoparticles (<<100 mg) to raise the temperature of a tumor mass (>1 g) to between 42 and 46 °C for a sustained period of time (>30 min).[19,25,26] Rational design of nanoparticles capable to realize such energy deposition with low-power AMFs has proven challenging. The complexity of the interplay between magnetic properties and crystal structure of the nanoparticles,[23,24] cooperative interactions among the nanoparticles,[27,28] and physiological constraints[26,28] are confounding factors that have inhibited progress, and which are overlooked by prevailing simple models.

Initial modeling efforts assumed nanoparticle colloid suspensions to comprise single-domain (or uniform magnetization) noninteracting magnetic cores.[13,23,29] These early efforts also constrained the analysis to a "linear-response" regime, limiting understanding of measured nonlinear responses.[30] Further experimentation, with polycrystallite core magnetic nanoparticles provided evidence that intercore magnetic (e.g., dipole–dipole) interactions can profoundly influence their loss behavior or heating rate.[23,24,27,28,31] Additional modeling provided a description of nonlinear behavior arising from interactions of single-domain magnetic nanoparticles possessing significant shape anisotropy.[23,32] The effect of solvent viscosity was also incorporated into models.[33] To date, the theoretical focus on single-domain ("monolithic" or uniform magnetization) magnetic crystallite core colloids has limited both understanding and innovation in synthesis processes to fully exploit the potential offered by polycrystallite core magnetic nanoparticles. We hypothesized that polycrystallite core magnetic nanoparticles offer added potential to modify the internal magnetic structure to realize specific performance criteria.[23,24,27] Magnetic nanoparticles intended for cancer hyperthermia must possess a sufficient magnetic response (i.e., nanoparticle magnetization) in order to generate therapeutic heat in the cancer before off-target heating creates unsafe temperatures in the patient.[23,25,26] Magnetic properties should also be managed to minimize agglomeration, while maintaining sufficient directional dependence to the magnetic response (magnetic anisotropy) for optimized loss power and heating.[23] The challenge, therefore, is to balance these, sometimes competing, structural and magnetic requirements while maintaining biocompatibility and stability under physiological conditions.[13,23] New experimental evidence is needed that correlates internal magnetic structure of nanoparticles with measurements of heating properties.

We report results of the first direct measurements of microscopic internal magnetic (intracore) structure from three magnetic iron oxide–dextran nanoparticle colloids. These domain characteristics are compared with measured structure, bulk magnetic properties under static magnetic fields, and loss power when the nanoparticles were exposed to AMFs. Microscopic magnetic properties were measured with polarization analyzed small angle neutron scattering (PASANS). Structure, composition, and magnetic properties were determined with X-ray diffractometry (XRD), transmission electron microscopy (TEM), dynamic light scattering (DLS), magnetometry, and Mössbauer spectroscopy. Amplitude-dependent heating properties were measured with fixed frequency (150 kHz) and varying peak amplitude (5–50 kA m$^{-1}$) AMFs.[30,34] Though nominally of similar structure, the three systems show dramatic differences in measured amplitude-dependent specific loss power (SLP(H)). Full characterization of the physical and magnetic properties of the particles reveals that differences of internal magnetic structure, not readily apparent from analysis of bulk structural and magnetic properties, are critical to differentiate heating behavior among the nanoparticles.

## 2. Results

All nanoparticles chosen for this study comprised dextran-stabilized magnetic iron oxide suspended in water, and were used as received. For clarity, we provide definitions of terminology we use to describe the nanoparticles. "Crystallite" refers to an individual crystal of iron oxide that can combine with others to form a nanoparticle "core." The core can be a solid core formed by a dense packing or aggregation of crystallites, or it may be a diffuse core formed by a loose packing of crystallites within a (polymer) matrix. Magnetic interactions can then occur between crystallites within a core (i.e., intracore) or between cores of neighboring nanoparticles (i.e., intercore). As a result, magnetic domains can form within a core, and may or may not correspond to the dimensions of a crystallite. Measured physical and chemical properties are summarized in **Table 1**. Bionized nanoferrite (BNF) nanoparticles obtained from micromod Partikeltechnologie, GmbH (Rostock, Germany) are synthesized by a high temperature, high pressure homogenization process to form a solid core composed of ordered iron oxide crystallites surrounded by a dextran shell (**Figure 1**, Column A, Row BNF).[35–37] JHU nanoparticles were synthesized by high gravity controlled precipitation, also forming a solid core of iron oxide crystallites surrounded by a dextran shell (Figure 1, Column A, Row JHU).[38,39] The third nanoparticle system chosen for study was commercial nanomag-D-spio (SPIO) particles obtained from micromod Partikeltechnologie, GmbH, which are synthesized by coprecipitation of iron salts in the presence of dextran.[40,41] Unlike the BNF and JHU colloids, nanomag-D-spio nanoparticles have a diffuse core formed by multiple crystallites dispersed in a dextran matrix, very similar to the most common magnetic iron oxide colloids used in medical imaging (Figure 1, Column A, Row SPIO).[13] All three systems share similar physico-chemical properties. They comprise a mixture of $Fe_3O_4$ and $\gamma$-$Fe_2O_3$ with a shell or matrix of dextran suspended in water, with a measured hydrodynamic (total particle) diameter of about 115 nm (Figure 1, Column B; and Table 1). The magnetic cores of the BNF and JHU nanoparticles comprise several crystallites of magnetic iron oxide aggregated to form a single dense core having nominal diameter of ≈50–60 nm as determined from TEM (Figure 1, Column C), analytical ultracentrifugation, and small angle neutron scattering (SANS) (see below).[24] Significant polydispersity (>0.3) is evident among all samples, which is a consequence of solution-based precipitation processes. TEM images of individual particles from each sample show some structural differences (i.e., shape, size, facet/edge effects) among the iron oxide crystallites, with BNF particle crystallites appearing largest (Figure 1 Column C). Few additional differences are observable among them, except perhaps a difference of the internal spatial configuration of the iron

**ADVANCED
FUNCTIONAL
MATERIALS**

www.afm-journal.de

*Materials
Views*

www.MaterialsViews.com

**Table 1.** Physical properties of nanoparticles.

| Particle[a] | Type | Particle conc. [mg mL$^{-1}$] | Fe conc. [mg mL$^{-1}$] | Mean particle diameter (PD)[b] [nm] | Iron oxide composition[c] $Fe_3O_4$/$\gamma$-$Fe_2O_3$/ $Fe(OH)_2$ %(±) | Shape of FeO crystals from SANS | Dimensions of iron oxide crystals [£,d] [nm(±)] | State of iron oxide crystals |
|---|---|---|---|---|---|---|---|---|
| BNF | Core–shell | 22 | 11 | 126 (39%) | 72(6)/ 28(5)/ ≈4 | Parallelepiped | 8(1) × 26(2) × 66(10) (SANS) 12(2) (XRD) 20 (TEM) | Aggregated into core |
| JHU | Core–shell | 64 | 9.2 | 117 (41%) | 76(9)/ 24(7)/0 | Spherical | 16(4) SANS) 9(1) (XRD) 15 (TEM) | Aggregated into core |
| Nanomag-D-spio | Polymer matrix | 96 | 12.5 | 106 (50%) | 87(7)/ 13(4)/0 | Spherical | 8.8(0.8) (SANS) 8(1) (XRD) 20 (TEM) | Crystallites clustered in small groups (2–3) and dispersed in dextran matrix |

[a]Error bars are 1σ unless otherwise indicated; [b]Mean diameter as measured by DLS, reported in nanometers. Diameter includes both iron oxide core and dextran shell. Polydispersity is the width of the distribution and is indicated in parentheses. (See the Supporting Information for more information.); [c]Iron oxide composition of core as measured by Mossbauer spectroscopy, reported as % of core total. (See the Supporting Information for more information.); [d]Dimensions ($L \times W \times H$ for parallelepipeds or diameter for spheres) as measured from polarized SANS, reported in nanometers. Note that fitting to unpolarized SANS data may produce different dimensions because magnetic and structural scattering are convoluted. Error bars are the larger of 1σ or the range of parameter values determined from fits of approximately equal quality (see the Supporting Information). Dimensions as measured from XRD using Scherrer peak analysis, reported in nanometers. (See the Supporting Information for more information.)

oxide crystallites (Figure 1C, and Table 1), with BNF and JHU appearing to comprise smaller cores (≈50 nm diameter) than nanomag-D-spio (≈100 nm); suggesting the former are dense whereas the latter is diffuse.

Overall, none of the three nanoparticle systems displays noteworthy differences in bulk DC magnetic properties (**Figure 2**A,C–E; **Table 2**; Supporting Information). The bulk magnetic data provide no clues to anticipate that the SLP, a
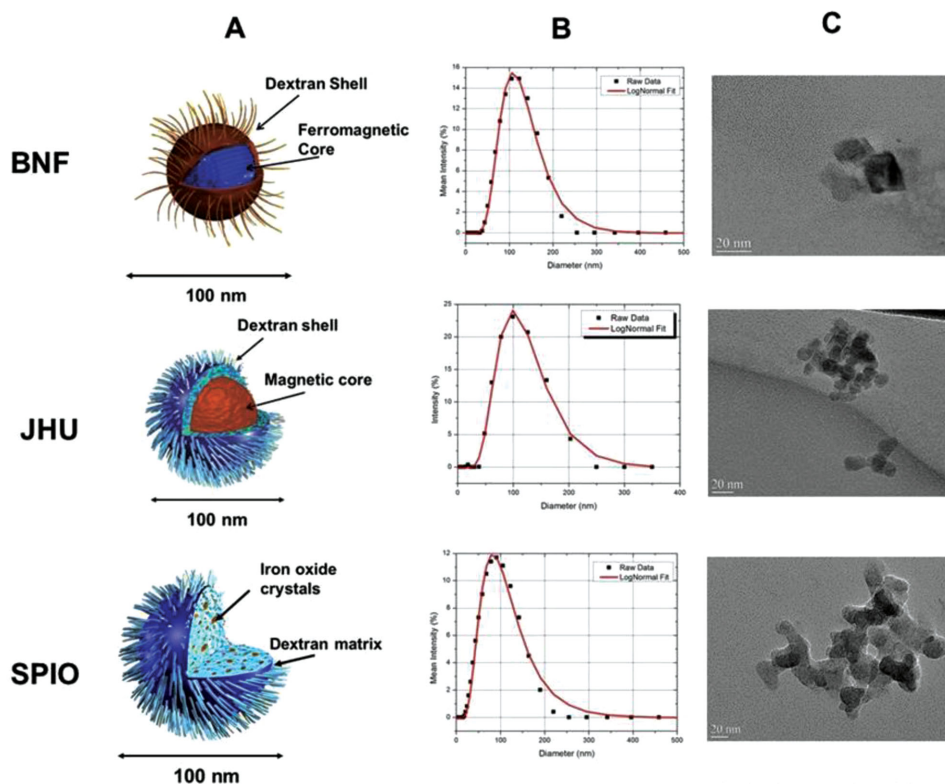


**Figure 1.** Schematic (Column A) and data (Columns B and C) showing physical properties of bionized nanoferrite (BNF) particles; JHU (JHU) particles; and, nanomag-D-spio (SPIO) particles used in the studies. Schematics of each particle (Column A) are provided to highlight key features of particle constructs. Column B: Intensity-weighted dynamic light scattering data of aqueous suspensions demonstrate roughly equivalent mean hydrodynamic diameter of particles. Column C: Transmission electron microscopy of nanoparticle shows each construct comprises multiple crystallites. Subtle variations among the crystallites and their spatial arrangements lead to complex micromagnetic structures that give rise to different time-dependent properties.
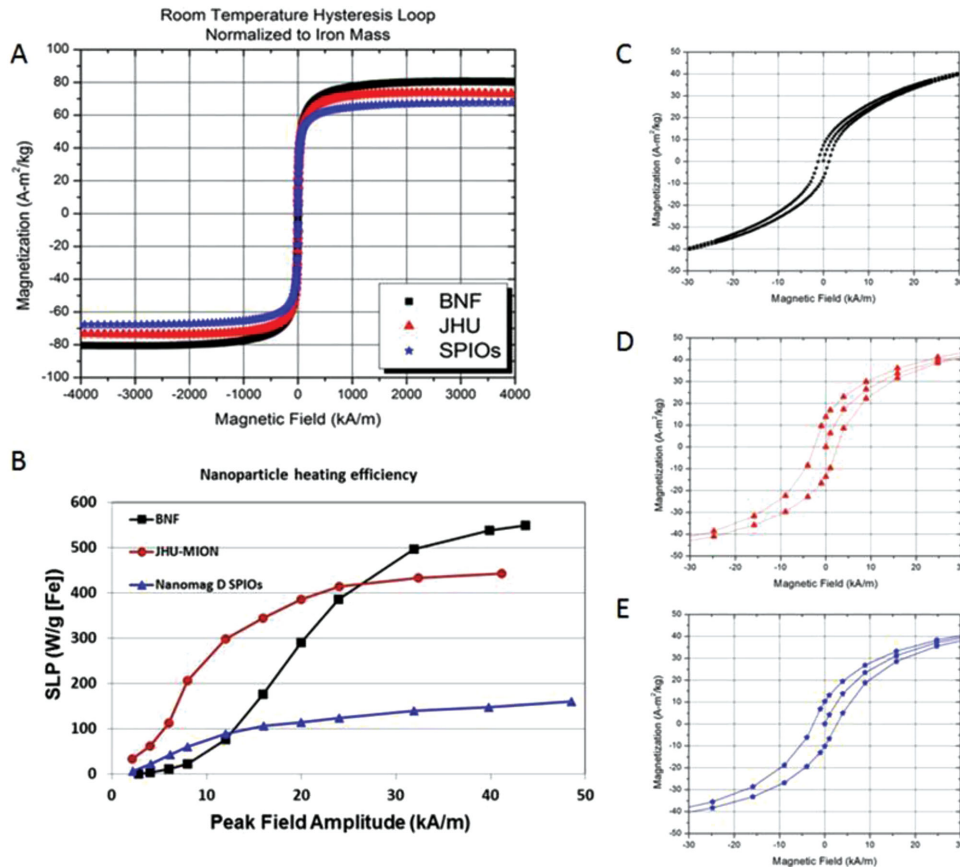
www.MaterialsViews.com

ADVANCED
FUNCTIONAL
MATERIALS
www.afm-journal.de

FULL PAPER

**Figure 2.** A) Normalized hysteresis loops of the BNF, JHU, and nanomag-D-spio nanoparticles in $H_2O$ at 300 K. Full hysteresis loop where the moment is normalized to the iron concentration. Sample holder and water contributions are removed, but contributions from the dextran remain. B) Specific loss power (SLP) of the BNF (black squares), JHU (red circles), and nanomag-D-spio (blue triangles) nanoparticles in $H_2O$ at 150 kHz as a function of peak magnetic field amplitude. The SLP is normalized to the iron concentration. C–E) Magnified view of measured hysteresis loops with virgin curves of the three nanoparticles. In all figures, error bars (1σ) are included, but may be smaller than the symbol.

measure of the heating rate in an applied AMF, would vary so dramatically among the samples (Figure 2B). All samples exhibit nonlinear amplitude-dependent response to applied AMF, with significant variations of both shape of heating curves and different amplitude at onset of plateau indicating saturation. The BNFs generate significant heat only when $H >$ 15 kA $m^{-1}$ (peak amplitude), but with the SLP still increasing past 500 W $g^{-1}$ Fe at >30 kA $m^{-1}$. By contrast, the JHU particles display significant heating at the lowest amplitude achieved (5 kA $m^{-1}$) which increases dramatically with increasing amplitudes exceeding heat output of BNF at 10 kA $m^{-1}$ by about

sixfold. Onset of a plateau occurs in JHU nanoparticles at about 440 W $g^{-1}$ Fe at 25 kA $m^{-1}$, earlier than observed for BNF nanoparticles. Finally, SLP measured from the nanomag-D-spios is the lowest overall and effectively plateaus at about 150 W $g^{-1}$ Fe for $H >$ 15 kA $m^{-1}$; however, it is noteworthy that heating from nanomag-D-spio nanoparticles exceeds that measured in BNF nanoparticles for amplitudes <15 kA $m^{-1}$. It is also worth noting that the nanoparticle systems do not exhibit a readily discernible linear response at amplitudes (>≈5 kA $m^{-1}$ peak amplitude) needed to generate nominal therapeutic heating (>50 W $g^{-1}$ Fe) (Figure 2B and the Supporting Information).

**Table 2.** Magnetic properties of nanoparticles.

| Particle[a] | Magnetization [A $m^2$ $kg^{-1}$ Fe(±)] | Magnetization [A $m^2$ $kg^{-1}$ particle(±)] | Effective anisotropy [J $kg^{-1}$ Fe(±)] | Minimum domain dimension parallel to guide field [nm(±)] | Minimum domain dimension perpendicular to guide field [nm(±)] |
|---|---|---|---|---|---|
| BNF | 80.76(0.06) | 19.86(0.02) | 0.4034(0.0004) | 20.8(0.4) | 7(2) |
| JHU | 73.6(0.1) | 10.558(0.001) | 0.511(0.004) | 36(2) | 14.0(0.4) |
| Nanomag-D-spio | 67.69(0.01) | 8.814(0.001) | 0.2708(0.0004) | 20 | 14.0(0.4) |

[a]Error bars are 1σ except in the case of magnetic domain sizes which were the larger of 1σ or the range of parameter values determined from fits of approximately equal quality (see the Supporting Information).

The measured saturation magnetization of the nanoparticles reveals only subtle differences. Saturation magnetization ($M_S$) of each magnetic colloid was measured at room temperature using superconducting quantum interference device (SQUID) magnetometry and normalized to the iron content (Figure 2A). Iron content was determined by inductively coupled plasma atomic emission spectroscopy (ICP-AES) (Table 1). Normalizing iron content among the samples enables comparison with the SLP. In short, $M_S$ varies by only 15% among the three samples (Figure 2A and Table 2). Close examination of nanoparticle magnetization in the low-field region (i.e., ±80 kA m$^{-1}$) also reveals only subtle differences in the shape of the hysteresis loops and coercivity (Figure 2C–E). These may be most readily attributed to either intercore dipolar interactions, different values for the intracore magnetic anisotropy, or a combination.[42] Interestingly, in all three cases, measureable SLP($H$) occurs when the magnetization is ≈40% of $M_S$ (Figure 2).

Magnetic dipole interactions have been an area of both experimental and theoretical investigations with evidence suggesting that dipolar interactions can either enhance or depress heating depending upon several factors including interparticle separation.[31,32] In a general way, dipolar interactions contribute to the collective anisotropy of the colloid, and these interactions correlate well with the heat generated with AMFs. Taken alone, however dipolar interactions insufficiently account for the onset and magnitude of heating observed in the current set of samples.[23] Using standard models, we might consider that the magnetic anisotropy of the colloid can be quantified through the anisotropy field ($H_k$), which can be determined directly from the peak positions measured using transverse susceptibility (Experimental Section and the Supporting Information).[43,44] In particular, we consider a model based on the work necessary to magnetize a unit volume of a magnetic material which is understood to be[45]

$$dW = \vec{H} \cdot d\vec{M} \tag{1}$$

where $H$ is the applied magnetic field and $M$ is the magnetization. Any net work performed is converted into heat ($W_{heat}$). This can be written as

$$W_{heat} = \oint \vec{H} \cdot d\vec{M} \tag{2}$$

The maximum heat ($W_{heat}^{max}$) generated by any magnetic system is the area enclosed by a square hysteresis loop

$$W_{heat}^{max} = 4 M_s \mu_0 H_k \tag{3}$$

Given that $\mu_0 H_k = 2K / M_s$, $W_{heat}^{max} = 8K$, the maximum power is $f W_{heat}^{max}$ where $f$ is the frequency of the applied magnetic field. Model calculations based on the values of $H_k$ obtained from our three systems predict that the highest measured SLP values ought to be obtained from JHU nanoparticles (see the Experimental Section). This prediction, however, is not borne out by measured SLP results (Figure 2B), which reveal that the BNFs generate the highest maximum heating rate at saturating (peak) amplitudes of >40 kA m$^{-1}$, although their low

amplitude heating (<15 kA m$^{-1}$) is well below that measured from JHU nanoparticles. Furthermore, when analyzing the SLP in the context of linear response theory,[29] it is clear that the SLP for the systems studied here is nonlinear (see the Supporting Information). While including dipolar interactions in theoretical models (notably as modifications to linear response theory)[23,31,32] has generally improved understanding of time-dependent processes in magnetic fine particle suspensions, it is clear that models developed to explain the observed amplitude-dependent heating rates must take into account additional factor(s) and/or limitations to explain nonlinear behavior.[46]

Certainly, an accounting of the source(s) of the unexpected heating differences among the samples should begin with considerations of chemical and crystal structure differences among the samples. Magnetite ($Fe_3O_4$) and maghemite ($\gamma$-$Fe_2O_3$) are both magnetic forms of iron oxide possessing slightly different crystalline and (bulk) magnetic properties. To that end, we examined the nanoparticles with Mössbauer spectroscopy and XRD to determine iron oxidation state and crystal structure, respectively (**Figure 3**). Analysis of the results shows that all three nanoparticle cores contain varying amounts of both magnetite ($Fe_3O_4$) and maghemite ($\gamma$-$Fe_2O_3$) crystals, as reported in Table 1. Ratios of $Fe_3O_4/\gamma$-$Fe_2O_3$ among samples may provide clues to subtle variations of micromagnetic states within the particles, providing some accounting for the varied responses to AMFs. Scherrer analysis (Figure 3C) of XRD data provides additional information to estimate mean crystallite size, which are similar among all samples. This analysis is potentially misleading because XRD is only sensitive to the smallest dimension of the crystallites comprising each nanoparticle core. Further characterization with additional techniques is needed to understand the internal crystallite and magnetic structures of the particles.

We chose to employ SANS to measure differences of magneto-structural properties among the nanoparticles. SANS is a powerful tool that can be used to directly probe the spatial relationship between atomic nuclei and magnetic volumes of nanostructured materials (**Figure 4**A).[47–50] Significant advantages offered by SANS include the ability to study nanoparticles suspended in biologically relevant media; and, the polarizable neutron spin which allows us to divide the magnetic scattering into orthogonal components—perpendicular ($\perp$) and parallel ($\parallel$)—to an applied external "guide" field, $H$ (i.e., $M^2_{PERP}$ and $M^2_{PARL}$) (Figure 4A and the Experimental Section).[48–50] Inclusion of such a polarization analysis (PASANS) of the neutron (magnetic) spin, coupled with recent significant advancements in polarization efficiencies and data analysis procedures, enables unambiguous and high-resolution studies of magnetic colloids often revealing unexpected results.[46,47] We utilized unpolarized SANS for nanoparticle suspensions to study the spatial relationship of nanoparticles in suspension (i.e., structural scattering, Figure 4B, and ref. [24]), and we later combined these results with PASANS (**Figure 5**) to analyze the internal magnetic structure of the iron oxide cores.

For BNF nanoparticles, analysis of the structure ($N^2$ data) reveals that each (dense) core comprises stacked ≈8 × 26 × 66 nm parallelepiped crystallites (Figures 1 and 4B, and Table 1). Magnetically, $M^2_{PERP}$ decreases sharply at higher scattering angle or wavevector, $Q \propto 2\pi/\text{length}$, than $M^2_{PARL}$
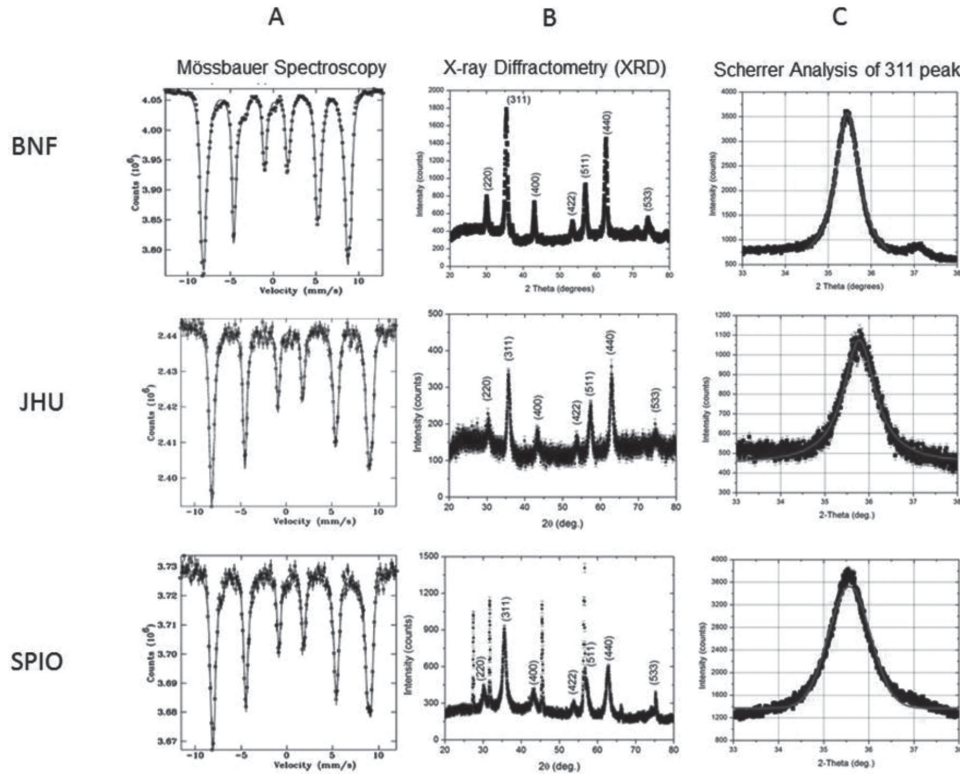
**Figure 3.** Physico-chemical characterization of nanoparticles as in Figure 1. Mössbauer spectroscopy (Column A) of bionized nanoferrite (BNF, first row); JHU (JHU, second row); and, nanomag-D-spio (SPIO, third row) nanoparticles demonstrates all comprise a mixture of $Fe_3O_4/\gamma\text{-}Fe_2O_3$ magnetic oxides of iron. Column B: X-ray diffractometry demonstrates highly crystalline compositions that are essentially similar among nanoparticle types; and, Column C: Scherrer analysis (311 peak shown) from XRD demonstrates that the mean crystallite size (smallest dimension) among the nanoparticles are similar.

(Figure 5A, Table 2). The parallelepiped model is most sensitive to the shortest dimension, thus careful fitting of the parallelepiped model to the data indicates that $M^2_{PARL}$ contains a minimum magnetic domain length of 21 nm which is notably larger than the minimum domain length in $M^2_{PERP}$ of only 7 nm. The shortest magnetic domain size of $M^2_{PERP}$ thus corresponds to the shortest structural crystallite size, whereas the shortest $M^2_{PARL}$ domain width is both longer than the shortest

structural crystallite edge, yet shorter than the longest crystallite dimension. Neutron scattering selection rules dictate that only the projection of $M^2 \perp Q$ can be measured. As shown in the Supporting Information, the composite magnetic structure displayed in Figure 5D results when this rule is combined with dipolar and Zeeman energetic considerations. Dipolar coupling between the crystallites favors alignment of the collinear component of magnetic moments along the same direction, while
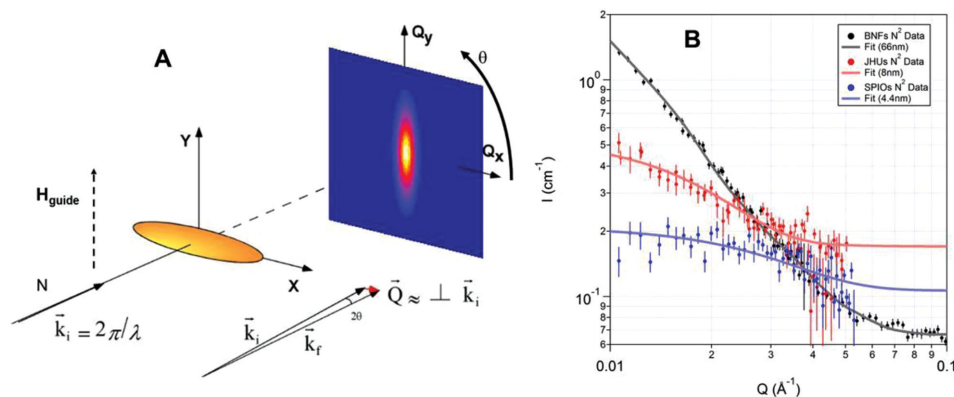


**Figure 4.** A) Schematic of the SANS configuration. B) Nuclear scattering only contribution to the polarized beam SANS data of the BNF, JHU, and nanomag-D-spio nanoparticles in $D_2O$ at room temperature along with fits. Error bars (1σ) are included, but may be smaller than the symbol.
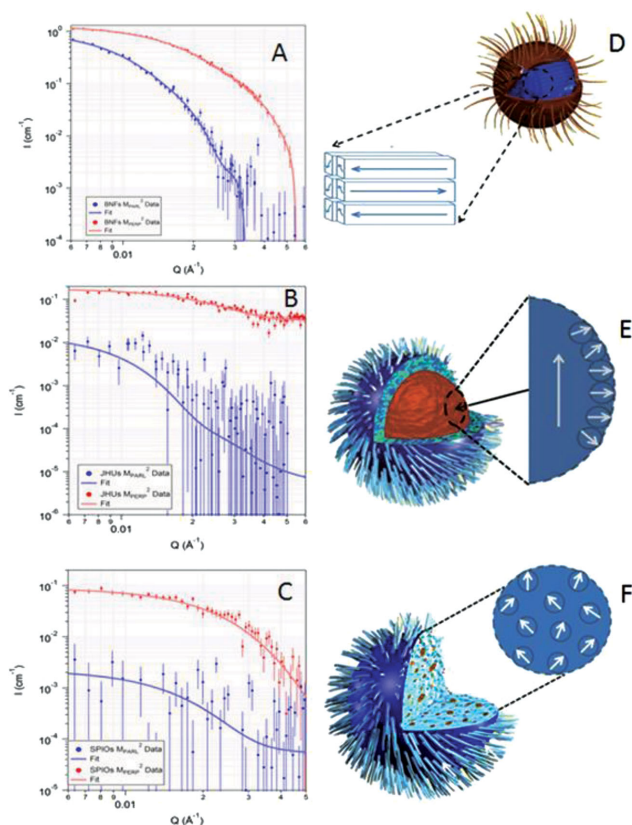
**ADVANCED
FUNCTIONAL
MATERIALS**

www.afm-journal.de

**FULL PAPER**

*Materials
Views*

www.MaterialsViews.com



**Figure 5.** Magnetic scattering contributions, (blue) parallel and (red) perpendicular, to the guide field with respect to the polarized beam SANS data of: A) BNF; B) JHU; and, C) nanomag-D-spio (SPIO) nanoparticles in $D_2O$ at room temperature. The fit shown uses models described in the text and illustrated in schematic diagrams. Domain structures of: D) BNF; E) JHU; and, F) nanomag-D-spio particles obtained from analysis and modeling PASANS data. Error bars ($1\sigma$) may be smaller than the symbol. Note scattered neutron intensity from JHU and nanomag-D-spio particles is lower than from BNF particles.

the side-by-side components of moments arrange antiparallel to one another. The latter antiparallel alignment conflicts with Zeeman energy considerations that favor a collinear alignment of all magnetic moments to an externally applied field. The magnetization components extracted from the PASANS results are consistent with the magnetic structure depicted in Figure 5D and explained in detail in the Supporting Information. The antiferromagnetic arrangement of the side-by-side moments persists for most of the random orientations of the crystallites relative to the applied field. When the small 1.2 kA m$^{-1}$ guide field happens to be oriented along the 8 nm crystallite dimension, however, the magnetization component along this short edge aligns parallel to the field (see the Supporting Information). Energy calculations described below (see Discussion) indicate that the dipole-induced antiferromagnetic arrangement of side-by-side moments are most easily overcome by a Zeeman-induced magnetic field applied along the shortest grain dimension (8 nm), followed by the medium dimension (26 nm), and then finally along the long crystallite axes (66 nm). Analysis of the PASANS data indicates that the small guide field used in the measurement is sufficient to align only the

moments along the shortest crystallite edge. This antiparallel (antiferromagnetic) coupling of structural crystallites differs from observations reported from other magnetic nanoparticle systems.[50]

Structural scattering, $N^2$, measured from JHU nanoparticles suggests that each core of ≈48 nm diameter comprises a collection of small, approximately spherical crystallites ≈16 nm diameter (Figure 4B, Table 1). Although $M^2_{PARL}$ and $M^2_{PERP}$ decrease at different values of $Q$ (Figure 5B), both can be described by a spherical model, yielding a magnetic domain structure that is ≈36 nm in diameter for the component of the magnetization parallel to the field and ≈14 nm in diameter for the perpendicular component. Fitting to the PASANS data is quite sensitive to the sphere radius in both cases with alternate values yielding predictions that deviate significantly from scattering data (Supporting Information). It is notable that the average domain dimension for $M^2_{PARL}$ in the JHU nanoparticles is approximately double the shortest domain dimension for $M^2_{PARL}$ in the BNFs (Table 2). Two magnetic models are consistent with the observed $M^2_{PARL}$ and $M^2_{PERP}$ scattering (Supporting Information) obtained from JHU nanoparticles. In the first model, we can consider that the cores have a "magnetic core/shell-like" structure with a "magnetic core" that is 36 nm diameter and coherently magnetized parallel to the guide field. The "magnetic shell" has an average thickness of about 7 nm (14 nm added to total diameter), that is broken into smaller subdomains magnetized perpendicular to the guide field (Figure 5E). In the alternate model, the individual structural crystallites may act as single magnetic domains, in which the parallel moments align through the majority of the core, but the perpendicular component varies from crystallite to crystallite. Micromagnetic simulations and neutron selection rules (see Discussion, Experimental Section, and the Supporting Information) support the former "magnetic core–shell" model (Figure 5E), thus allowing us to exclude the latter from consideration.

The nuclear scattering component, $N^2$, obtained from the nanomag-D-spio nanoparticles is well described by a collection of independent (approximately spherical) crystallites of ≈9 nm diameter that form aggregated diffuse "core," in which the crystallites are dispersed throughout the polymer nanoparticle (diameter ≈100 nm) matrix (Figures 4B and 5F). In contrast to results obtained from BNF and JHU nanoparticles described above, the net $M^2_{PARL}$ is only slightly higher than background and our attempts to extract a value for $M^2_{PARL}$ via a subtraction method produced no measureable magnetic moment (shown in the Supporting Information);[48,49] but, it is reasonable to assume that the magnetic domain size parallel to the field is commensurate with the measured nuclear crystallite size from SANS (Figures 4B and 5C). The magnetic scattering perpendicular to the field is statistically significant (Figure 5C), and can be modeled as spherical domains of 14 nm in diameter, which is consistent with the average cluster size of 2–3 crystallites (from TEM, Figure 1). This domain structure is shown graphically in Figure 5F.

## 3. Discussion

The dramatic variations observed in the magnitude, onset, and slope of the SLP($H$) (Figure 2B) for the three magnetic iron

www.MaterialsViews.com

www.afm-journal.de

ADVANCED
FUNCTIONAL
MATERIALS

FULL PAPER

oxide nanoparticle colloids studied cannot be explained by the measured (subtle) differences of their overall magnetic properties, such as $M_s$ and $K_{eff}$ (Table 2). Furthermore, it is worth noting that this result is contrary to model predictions in which these magnetic properties are considered the dominant contributing factors to SLP.[23,29] The observed differences of SLP are consistent with recent observations comparing intercore dipole–dipole interactions between BNF particles and manganese-doped ferrites[31] with different chemical and magnetic characteristics. It is striking that our three particle systems possess nearly identical physico-chemical features (Figures 1–3, Tables 1 and 2) and one might expect that the intracore magnetic structure would be similar among them. Indeed, SLP measurements limited to low amplitude (<10 kA m$^{-1}$) would generally support conclusions reached from both bulk measurements and existing models. Such limited measurement range provides little indication that significant differences exist among the nanoparticles,[30] and it is reasonable to ask whether additional and previously unaccounted factor(s) dominate the SLP($H$).

When a suspension of magnetic nanoparticles is subjected to an AC magnetic field or AMF, the individual moments comprising each core are forced to rapidly reorient to align with the applied magnetic field, provided the amplitude of the field is sufficient to overcome any core magnetic anisotropy.[23,51] It is worth emphasizing that Brownian relaxation or mechanical motion of the nanoparticles is unlikely to contribute significantly to particle magnetization reorientation in our current system because the time scale of the external magnetic field oscillations, ≈6 × 10$^{-6}$ s (150 kHz), exceeds the time scale of Brownian relaxation processes for a 100 nm diameter particle in water, ≈1 × 10$^{-3}$ s (1 kHz).[23] For most applications, AMFs are symmetric about zero field ($H = 0$), and so the complex magnetic domain structure revealed by the PASANS measurements (Figure 5D–F) at (or very near) zero applied magnetic field highlights the reorientation of the moment within each core that must occur during magnetic reversal. Since an AC field cycle would be expected to change the domain structure present, DC characterization has limited application to AC characterization. However, in these samples it is not an unreasonable assumption that the intracore domain structure is robust regardless of AC field amplitude. This is due to the low $M_S$ and low $H_C$ in these samples (Figure 2). Our bulk magnetization measurements (Figure 2) revealed that remanent magnetization measured for all nanoparticles samples studied was small relative to their saturation magnetization and the saturating field >1000 kA m$^{-1}$ (12 500 Oe). In contrast, the maximum amplitude AC field that was applied was less than 50 kA m$^{-1}$ (625 Oe), thus the samples were exposed to fields well below saturating field amplitudes. In addition, DC coercivity was observed to be very low and the measured virgin magnetization curves demonstrated similar (although not identical) behavior with the ascending and descending arms of the hysteresis loop (Figure 2C–E). Furthermore, we empirically determined that SANS data obtained from virgin samples in zero field were essentially identical to those obtained after magnetization in ±1200 kA m$^{-1}$ (1500 Oe). Finally, SLP versus peak field amplitude was measured to be the same when measured with increasing or decreasing fields. Therefore, it is clear that the

internal magnetic structure, which differs significantly among the particles, is a critical feature responsible for both the mechanism of reorientation and the resulting energy dissipation.

Based upon the physical characteristics of the BNF, JHU, and SPIO nanoparticles determined from XRD, Mossbauer, and PASANS, we identified and estimated the magnitude of the primary competing energy contributions (i.e., Zeeman, dipole, anisotropy, exchange interactions, etc.) for each nanoparticle system. We then used these estimates as input data for object oriented micromagnetic framework (OOMMF) simulations of the micromagnetic structure and explored the relative importance of each of these energy contributions to determine the magnetic behavior of each colloid system.[52]

The BNF nanoparticles, having a dense, polycrystallite core comprising long, slender structural crystallites, exhibit a high saturation magnetization. Magnetocrystalline anisotropy of magnetite, which in this case also includes a shape anisotropy contribution, dictates that in very low fields and at room temperature the ferrimagnetic moments align along the (111) crystal axis or equivalent direction. On average, this implies that each parallelepiped-shaped crystallite will contain a preferred magnetic orientation with a projection along each of its coordinate axes. The lowest energy configuration for dipolar coupling among such crystallites is obtained only when the magnetic component of each crystallite pointed toward a neighboring crystallite assumes a common direction with other similar components (Figure 5D); and, simultaneously the magnetic components that are aligned side-by-side (Figure 5D) are coupled in an antiparallel manner. Small magnetic fields of 1.2 kA m$^{-1}$ are only able to overcome this antiparallel coupling along the shortest dimension (8 nm); the 26 and 66 nm dimensions would require increasingly larger applied fields to overcome their antiferromagnetic arrangements (Supporting Information). Additionally, OOMMF simulations which include Zeeman, dipole, and anisotropy energy interactions also predict a model of antiparallel coupling along the longest two axes at small applied magnetic fields (Supporting Information).

Although the magnetic domain structure imposed by the parallelepiped crystallite structure of each BNF nanoparticle is complex, the magnetization within the entire nanoparticle must be fully aligned at the maximum field amplitude to generate the maximum SLP (see Equation (3)). Thus, BNF nanoparticles exposed to the applied field must first overcome dipolar coupling and demagnetizing fields internal to the core. Larger fields are required to produce the net magnetization responsible for the intercore dipole–dipole interactions leading to previously observed colloidal clustering.[23,24,27,28] The strong intracore coupling can also account for enhanced intercore interactions that require a higher field to initiate significant heating.[31,32] This behavior (delayed onset and plateau) is in qualitative agreement with the model developed by Kashevsky et al. describing hysteresis heating of acicular particles having a large uniaxial anisotropy.[32]

By contrast, the OOMMF simulations predict that the JHU nanoparticles (Supporting Information) comprise a central, magnetically coherent core with an effective shell of perpendicular (or canted) spins along the edges. This model agrees qualitatively with an interpretation of PASANS data for a ≈36 nm diameter core having magnetization aligned parallel to the

external field with a 7 nm thick "shell" with a canted magnetization (Figure 5E). In this system, the magneto-crystalline anisotropy is one of the dominant contributions to the energetics because the demagnetizing field and shape anisotropy are insignificant within the smaller (shell) spherical crystallites. The JHU cores display a larger anisotropy (by ≈20%) and slightly lower saturation magnetization (9% less) than the BNFs. The differences in saturation magnetization, anisotropy, and crystallite shape may permit the crystallites to be less coupled through magnetic exchange interactions (and therefore easier to align in a smaller magnetic field) than those of the BNFs. This difference produces a lower onset of significant SLP($H$) than observed for the BNFs. In a sense, limited oxidation of magnetite to maghemite led to attenuated coupling producing an effect on SLP behavior that is similar to that observed with doping magnetite to produce manganese ferrites.[31] However, the "magnetic core/shell-like" structure is expected to be more difficult to saturate fully than the coupled parallelepiped crystallites within the BNFs, leading to a lower maximum SLP($H$) generated by the JHUs at the AMFs accessible. This unusual structure and the resulting response to AMF have not been previously described by theoretical models.

Finally, absence of a coherent intracore magnetization (from coalesced crystallites) in the nanomag-D-spio nanoparticles suggests that the individual crystallites of iron oxide are spatially separated within the dextran matrix and thus are likely weakly coupled single magnetic domains. In this system, the magnetic domains are confined to the boundaries of an individual structural crystallite or cluster (Figure 5F). Less energy is required to magnetize these noninteracting crystallite clusters, and thus these nanoparticles display the lowest onset of measurable SLP($H$). Conversely, the weak intercore magnetic interactions produce little dipole interaction to enhance the anisotropy, and the nanoparticles produce only modest heating when exposed to AMFs. In general, this nanoparticle type is representative of colloidal iron oxides most commonly used in medical applications to date, and most closely resembles theoretical constructs.

## 4. Conclusion

To conclude, insufficient characterization of bulk and microscopic properties (static and dynamic) of magnetic colloids has inhibited progress toward an understanding of these complex systems. This issue is particularly evident for in vivo medical applications which place high demands on material performance. SLP measurements limited to amplitudes below saturation typically fail to demonstrate the nonlinearity of SLP($H$), justifying continued use of models that fail to fully describe the complexities of the interplay among intra- and intercore features. Recent observations by multiple research groups, including ours have demonstrated the importance of intercore dipole interactions for heating performance.[23,24,27,28,30–32] In this work, we have explored the observation that variations in measured values of the SLP($H$) exhibited by nanoparticles demonstrating similar bulk magnetic and structural characteristics arise from variations of internal magnetic (intracore) structure. These intracore magnetic interactions must also be considered when tailoring nanoparticle synthesis for a desired end-use in

order to strike a balance among interaction strength, exchange coupling, and external magnetic field. Our results suggest a renewed examination of models and characterization methods is needed to advance magnetic colloids for various applications.

## 5. Experimental Section

*Sample History*: For every measurement made (PASANS, SQUID, transverse susceptometry, DLS, SLP, etc.), a fresh sample was prepared from the same original lot used for study, after vortex mixing to ensure homogeneity. Thus, no sample had been previously frozen or exposed to a magnetic field (either AC or DC) from previous measurements prior to a measurement (unless otherwise specified). In this way, it was sought to avoid issues such as change in concentration due to chaining or interaction with container, contamination, magnetic field history changing domain structure, etc.

*Particle Size Analysis by Dynamic Light Scattering (DLS)*: The hydrodynamic diameter of the $Fe_3O_4$/$\gamma$-$Fe_2O_3$ particles was measured by Horiba LB-550 Dynamic Light Scattering Particle Size Distribution Analyzer[36] with 0.01 wt% iron oxide aqueous suspension. The distribution base was set to volume mode and the refractive index of $Fe_3O_4$ and DI water were set at 2.42 and 1.33, respectively. DLS provides a measure of the hydrodynamic size based on assumptions of light scattering from a spherical object having a uniform density. DLS data from the systems include significant contribution from the dextran, which in water exhibiting a "swollen" conformation with significant solvent (water) molecule penetration. A distribution can be obtained from these data, which is reported as polydispersity in Table 1.

*Tunneling Electron Microscopy (TEM) and Scanning Electron Microscope (SEM)*: The TEM images were acquired on a 200 kV JEOL 2010 transmission electron microscope.[36] The specimens were prepared by placing a drop of suspension containing a drop of aqueous $Fe_3O_4$/$\gamma$-$Fe_2O_3$ (3 mass%) in 20 mL methanol onto a carbon coated copper grid followed by drying at room temperature for 24 h. The size and morphology of the samples were also investigated with a KYKY-2800B SEM.[36] TEM provides information on the core size (which is a collection of crystallites), but the crystallites are difficult to identify and analyze without adequate spacing. Distribution information obtained from TEM is complicated significantly by the "coffee ring" phenomena present in all dried nanoparticle systems, which makes it difficult to unambiguously distinguish individual cores or crystallites. The utility of TEM is therefore limited when characterizing and comparing the intercrystallite spatial arrangements of/among these iron oxide/dextran nanoparticles.

*X-Ray Diffractometry (XRD) and Analysis*: The crystal structure and crystallite size of the samples were examined by powder XRD on a Philips Norelco diffractometer (type 42273/1, Mount Vernon, NY)[36] with Cu K$\alpha$ radiation at room temperature. The diffractometer is equipped with incident Soller slits, a theta-compensating slit, and graphite monochromator, and a scintillation detector. XRD was performed on powdered samples over the 2$\theta$ range of 20°–80° with a step width of 0.005° and a sampling time of 4 s. Intensity data measured as relative peak heights above background were obtained using the DATASCAN software package.[36] Size was determined using Scherrer analysis of the peaks, which were fit to Lorentzian (BNFs and JHUs) or Gaussian (SPIOs) functions. While Scherrer analysis yields a measure of crystallite size, however it yields the small dimension of the crystallite. It is thus impossible to resolve a distribution from these data, as the smallest dimension yields the largest broadening, confounding contributions from larger crystallites.

*Mössbauer Spectroscopy*: The composition of the samples was determined by $^{57}$Fe transmission Mössbauer spectroscopy using a constant acceleration spectrometer calibrated with $\alpha$-Fe at room temperature and a 1 GBq $^{57}$CoRh source. Spectra were collected with the samples in a Janis SHI-850 closed cycle refrigeration system[36] at 10 K.

*Magnetometry*: Hysteresis loops were measured at temperatures ranging between 300 and 5 K from ±5570 kA m$^{-1}$ (±70 000 Oe) using

a superconducting quantum interference device vibrating sample magnetometer (SQUID VSM) from Quantum Design, Inc.[36] The colloidal samples were loaded into Kel-F liquid capsules from LakeShore Cryogenics,[36] and sealed with epoxy to prevent evaporation of the water solvent during measurement under vacuum. Background data due to sample holders and water were subtracted from sample data, but a contribution from dextran contribution remained. Flux trapping in the superconducting magnet is $\pm2.4$ kA m$^{-1}$ (30 Oe). This was not subtracted.

*Transverse Magnetic Susceptibility*: In a Janis Super-VariTemp Cryostat with a split-core 5 T superconducting magnet,[36] the transverse susceptibility was measured at 5 K (for signal to noise) using a self-resonant circuit operating at $\approx1.5$ MHz, where the AC magnetic field was applied perpendicular to the DC magnetic field. The location of the peaks in the transverse susceptibility corresponded to the effective anisotropy field ($H_k$) of the nanoparticles. The measured anisotropy field (see the Supporting Information for susceptibility data) for the BNFs was $\mu_0 H_k = 10$ mT; $\mu_0 H_k = 14$ mT for the JHUs; and, for the nanomag-D-spio nanoparticles, $\mu_0 H_k = 8$ mT. Given $\mu_0 H_k = 2K_{eff}/M_s$, when normalized to iron concentration, the effective anisotropy ($K_{eff}$) was $4.034(4) \times 10^{-4}$ J kg$^{-1}$ of Fe, $5.11(4) \times 10^{-4}$ J kg$^{-1}$ of Fe, and $2.708(4) \times 10^{-4}$ J kg$^{-1}$ of Fe for the BNF, JHU, and nanomag-D-spio nanoparticles, respectively. As the maximum work done in a magnetic system is $8K_{eff}$ (assuming square hysteresis loops, see Equation (3)), more heat is generated (or more work is performed) for larger values of the anisotropy.

*Small Angle Neutron Scattering (SANS)*: The SANS measurements were performed at the National Institute of Standards and Technology (NIST) Center for Neutron Research on the NG-3 beamline at room temperature. The utility of neutrons for scattering studies arises because they are electrically neutral and possess both mass and a small magnetic moment. Therefore, neutrons will scatter from the nuclei of material (nuclear scattering) via the short-range strong nuclear force or from unpaired electrons in magnetic materials (magnetic scattering) via the dipole–dipole interaction. Careful choice of the experimental conditions, i.e., sample (iron oxide nanoparticles) and solvent (D$_2$O), allows us to highlight specific features such as the magnetic scattering. Neutron selection rules dictate that the scattered neutrons are sensitive only to the projection of the magnetization that is perpendicular to the scattering vector $Q$. This constraint and other complexities necessitate use of spin (magnetic moment) polarized neutrons to enable unambiguous isolation of the magnetic scattering from the background scattering and determination of the vector components of the magnetization. For PASANS, additional modifications to experiment and equipment were needed. To begin, the neutron polarization (magnetic) spin state can be defined as either + or −. Thus, a measurement of all four possible neutron spin cross sections (++, +−, −+, and −−) allows for the unique separation of nuclear scattering ($N^2$) from magnetic scattering, irrespective of whether the sample is magnetically saturated. Simply, the "+ to +" and "− to −" scattering (or nonspin–flip scattering) contains information describing nuclear scattering and magnetic scattering predominantly from moments parallel to the applied sample field, whereas "+ to −" and "− to +" (or spin–flip scattering) contains only magnetic scattering. The complete, angle-dependent polarization selection rules become simplified at specific angular positions on the 2D detector (Figure 4A). Specifically, the nuclear scattering ($N^2$) can be separated from the scattering from net moments parallel to the magnetic "guide" field ($M^2_Y = M^2_{PARL}$) and those moments perpendicular to the applied guide field ($M^2_{PERP}$ which is a linear combination of $M^2_X$ and $M^2_Z$). Note that $M^2_{PARL}$ is described as the net magnetic moment. Beginning with the corrected[48,49] 2D scattering patterns (see Figure 4A) from the magnetic nanoparticles in the 1.2 kA m$^{-1}$ field parallel to the $Y$-axis, area-normalized sector slices of $\pm10°$ are taken about $\theta = 0°$, where $\theta$ is the angle between the $X$-axis (horizontal midline of the detector) and the projection of the scattering vector, $Q$, onto the $X–Y$ detector plane. At this angle, $M^2_{PERP} = M^2_Z$. Note that $M_Z = M_X$ is assumed by symmetry. Unpolarized SANS data were taken with 0.84 nm wavelength neutrons in transmission using three detector settings in order to span the range of scattering vectors $Q$ from $3 \times 10^{-5}$ to $5 \times 10^{-1}$ Å$^{-1}$. For PASANS, to cover

the necessary $Q$ range of (0.005–0.2) Å$^{-1}$ for the BNFs, two different wavelengths of neutrons were used: (5 ± 0.6) and (7.5 ± 0.9) Å. The 5 Å (7.5 Å) neutrons were polarized with an efficiency of 0.888 ± 0.005 (0.935 ± 0.003) by scattering from an FeSi supermirror, transmitting the spin-up (+) neutrons through the beam guide. Prior to interaction with the sample, the incident neutron polarization direction can be reversed at any time using an electromagnetic flipper coil with a flipping efficiency of 0.988 ± 0.004 (0.979 ± 0.003). For the JHUs and nanomag-D-spios, only the (7.5 ± 0.8) Å neutrons were used to cover the necessary $Q$ range of (0.005–0.06) Å$^{-1}$. The 7.5 Å neutrons were polarized with an efficiency of 0.95 ± 0.02 with the FeSi supermirror, and the electromagnetic flipper coil had a flipping efficiency of 0.975 ± 0.009. After scattering from the sample of interest, an analyzing glass cell filled with polarized $^3$He gas preferentially transmits neutrons with spins aligned parallel to the $^3$He atoms, while neutrons of the other spin state are absorbed. The orientation of the $^3$He spin filter can also be reversed at any time with a nuclear magnetic resonance pulse having an appropriate frequency. The data are then corrected for detector efficiency, background, and the polarization efficiency plus the time dependence of the $^3$He cell according to previously described methods.[48–50]

*OOMMF Simulations*: OOMMF is a portable, extensible public domain micromagnetic program developed at the NIST.[52] These micromagnetic computations solve for the minimum energy configuration of spins in a magnetic material, using the Landau–Lifshitz–Gilbert equation and the sum of the exchange, anisotropy, demagnetization, and Zeeman energy densities ($E_{density}$)

$$\frac{dM}{dt} = \frac{-\omega}{1+\lambda^2}M \times H_{eff} - \frac{\lambda\omega}{(1+\lambda^2)M_S}M \times (M \times H_{eff})$$

where $H_{eff} = \frac{-1}{\mu_0}\frac{\partial E_{density}}{\partial M}$ is the permeability of free space, $M$ is the magnetization, $t$ is time, $M_S$ is the saturation magnetization, $\omega$ is the phenomenological precession parameter, and $\lambda$ is the phenomenological damping parameter. Anisotropy, applied field, and initial magnetization can be varied pointwise, and arbitrary shaped elements can be modeled. For our simulations, the OOMMF code was further modified to enable calculation of Zeeman and dipole interaction energies. In all OOMMF magnetic simulations,[52] we used the bulk volume magnetization value of magnetite ($M_S$) of $5.05 \times 10^5$ A m$^{-1}$. The bulk volume (mass, assuming bulk density of magnetite) magnetocrystalline anisotropy value ($K$) of magnetite at room temperature is $K_1 = -1.35 \times 10^4$ J m$^{-3}$ (−1.88 J kg$^{-1}$ of Fe) and $K_2 = -0.44 \times 10^4$ J m$^{-3}$ (0.61 J kg$^{-1}$ of Fe), yielding easy axes along the (111) and equivalent directions. For simplicity in these simulations we manually fixed $K$ to be $+1.35 \times 10^4$ J m$^{-3}$ (1.88 J kg$^{-1}$ of Fe) which has the effect of denoting a single, uniaxial easy axis. The BNF cores, which are comprised of long and slender parallelepiped crystallites, are assumed to have the (100) axis along the short edge (8 nm), the (010) along the second longest edge (26 nm), and the (001) along the longest edge (66 nm). The magneto-crystalline anisotropy direction is randomly distributed along the (111) and equivalent crystalline axis. The JHU cores, by contrast, do not have such well-defined subcrystallites. In this case, it is assumed that the JHU cores can reorient such that their easy axis coincides with the applied magnetic field. We additionally consider the case in which the magnetocrystalline axis is held fixed at a 45° angle with respect to the applied field, but the results of these simulations did not match with experiment. The BNF cores are subdivided into 2 nm cubes that approximate the parallelepiped crystallites with a slight gap between crystallites (see the Supporting Information). The JHU cores are also subdivided into 2 nm cubes that approximate particles having 48 nm diameter dense cores (see the Supporting Information). Each subunit contains one net spin. The exchange constant for magnetite is nominally $1.3 \times 10^{-11}$ J m$^{-1}$. However, because we consider single-spin blocks (2 nm) that are significantly larger than the formula unit of magnetite at 0.84 nm (containing 24 Fe atoms and 32 O atoms), it is reasonable to reduce the effective nearest neighbor exchange constant by a factor of about 100. Without such a reduction, the simulations

**FULL PAPER**

fail to match experimental data. Thus, the OOMMF simulations are primarily sensitive to dipolar, Zeeman, and magnetocrystalline anisotropy contributions. OOMMF simulations for the BNF cores show a distinctive tendency to align antiparallel along their longest crystallite axes. The crystallites also have a tendency to align parallel along directions for which crystallites are pointing toward one another. Both of these traits agree well with the dipolar and Zeeman energy results obtained from simple calculations of Zeeman and dipolar energies (see the Supporting Information), and agree well with experimental PASANS results. OOMMF simulations for the JHU cores produce a domain with moments parallel to the guide field of length ≈30 nm plus smaller domains with moments perpendicular to the guide field located toward the core edges (see the Supporting Information). Both of these length scales agree with experimental PASANS results. We cannot rule out the possibility that the JHU nanoparticles have additional internal structure that we have not taken into account in the modeling.

*Iron Concentration Measurement by ICP-AES*: The final concentration of $Fe_3O_4/\gamma$-$Fe_2O_3$ in the aqueous suspension was obtained by dual-view Optima 5300 DV ICP-AES system.[36] The samples are all thoroughly washed to remove any unreacted materials prior to any characterization. Therefore, additional washing is unnecessary prior to ICP-AES. The sample digestion and preparation were done based on the Milestone microwave laboratory system.

*Alternating Magnetic Field (AMF) Equipment and Specific Loss Power (SLP) Measurements*: The AMF system comprises three main components: (a) the power supply; (b) an external impedance matching (capacitance) network; and, (c) the load which is a modified solenoid inductor having a vertical configuration.[30,34] The power supply was an 80 kW induction heating system manufactured by PPECO (Watsonville, CA) providing alternating current with variable frequency between 135 and 440 kHz, which was adjusted for stable oscillation at 150 ± 5 kHz.[36] To ensure accurate estimates of the SLP, the solenoid was constructed to encompass the entire sample volume in a homogenous field.[33] The coil has four turns formed from cylindrical sections of copper plate along with other design elements that enhance performance over a comparable solenoid. The magnetic field amplitude was measured with AMF Life Systems, Inc. field probes[36] and solenoid calibrations were performed with copper wire.[53] The probe was also used to measure the axial component of the field produced over the length of the coil (≈16 cm). With 650 V applied to the coil at 141 kHz maximum magnetic field amplitude of 47.9 ± 0.2 kA m$^{-1}$ (peak) and a range of uniformity (≥10% of peak) were measured over a length of 6.6 ± 0.3 cm. The magneto-thermal calorimeter is comprised of an insulating sample holder placed within the solenoid induction coil.[30] The SLP measurements were performed as previously described.[30] Briefly, 1 mL volumes of sample (nanoparticle suspension) or water were placed in standard 12 mm (5 mL) polystyrene test tubes and inserted into the insulated chamber. The rate of temperature rise for suspensions and water (for blank correction) were measured at 1 s intervals with a FISO Technologies Ltd. fiber-optic temperature probe.[36] Samples were tested with varying AMF amplitude ranging from 0 to 50 kA m$^{-1}$ (peak) at a frequency of 155 ± 5 kHz. After thermal equilibrium between the sample and calorimeter was established, the AMF power was applied and maintained for at least 30 s or until a sample temperature of ≈70 °C was achieved. Temperature measurements from a "water blank" containing 1 mL of distilled water were also taken at each power setting, and subtracted from sample temperatures to correct for calorimeter heat capacity, as follows. To calculate the SLP, the temperature obtained at each time step, $T_n$, was subtracted from the initial temperature, $T_0$, to yield $\Delta T_n = T_n - T_0$ data. Water blank $\Delta T$ values were subtracted from the sample $\Delta T$ values to obtain the corrected temperature change for each sample. The SLP was estimated from the initial and steepest part of the slope, $\Delta T/\Delta t$, of the time–temperature curve. The appropriate interval for calculating the slope was determined by analyzing a plot of the incremental temperature change, an analogue of the first derivative of the $\Delta T$ versus $\Delta t$ data, for each data set. The change in temperature between each time step and the immediately preceding time step was calculated, i.e.,

$T_n - T_{n-1}$ and these data were plotted versus $t$. SLP was then calculated as $SLP = C / m_{Fe}(dT / dt)|_{t\to0}$, where $m_{Fe}$ is the mass of iron in the sample for iron oxide–based nanoparticles; $C$ is the heat capacity of the sample (assumed to be that of water or 4.18 J g$^{-1}$ °C); and, $\Delta T/\Delta t$ is the measured rate of temperature rise ($\Delta T$) during the heating interval ($\Delta t$) or $T_n - T_{n-1}$ versus $\Delta t$.[30]

## Supporting Information

Supporting Information is available from the Wiley Online Library or from the author.

[1] N. F. Putman, K. J. Lohmann, E. M. Putman, T. P. Quinn, A. P. Klimley, D. L. G. Noakes, *Curr. Biol.* **2013**, *23*, 312.

[2] C. Corot, P. Robert, J.-M Idée, M. Port, *Adv. Drug Delivery Rev.* **2006**, *58*, 1471.

[3] B. D. Terris, T. Thomson, *J. Phys. D: Appl. Phys.* **2005**, *38*, R199.

[4] I. Žutić, J. Fabian, S. Das Sarma, *Rev. Mod. Phys.* **2004**, *76*, 323.

[5] K. Raj, R. Moskowitz, *IEEE Trans. Magn.* **1980**, *16*, 358.

[6] E. Hopkins, *On the Connexion of Geology with Terrestrial Magnetism: Showing the General Polarity of Matter, the Meridional Structure of the Crystalline Rocks, their Transitions, Movements and Dislocations, Including the Sedimentary Rocks, the Laws Regulating the Distribution of Metalliferous Formations, and Other Magnetic Phenomena*, Richard and John Edward Taylor, London **1844**.

[7] H. Shao, C. Min, D. Issadore, M. Liong, T. J. Yoon, R. Weissleder, H. Lee, *Theranostics* **2012**, *2*, 55.

[8] M. Swierczewska, S. Lee, X. Y. Chen, *Mol. Imaging* **2011**, *10*, 3.

[9] B. Gleich, R. Weizenecker, *Nature* **2005**, *435*, 1214.

[10] S. J. DeNardo, G. L. DeNardo, L. A. Miers, A. Natarajan, G. N. Adamson, C. Gruettner, R. Ivkov, *Clin. Cancer Res.* **2005**, *11*, 7087s.

[11] S. J. DeNardo, G. L. DeNardo, A. Natarajan, L. A. Miers, A. R. Foreman, C. Gruettner, G. N. Adamson, R. Ivkov, *J. Nucl. Med.* **2007**, *48*, 437.

[12] J. Kim, J. E. Lee, S. H. Lee, J. H. Yu, J. H. Lee, T. G. Park, T. Hyeon, *Adv. Mater.* **2008**, *20*, 478.

[13] Q. A. Pankhurst, N. T. K. Thanh, S. K. Jones, J. Dobson, *J. Phys. D: Appl. Phys.* **2009**, *42*, 224001.

[14] M. S. Goldberg, S. S. Hook, A. Z. Wang, J. W. M. Bulte, A. K. Patri, F. M. Uckun, V. L. Cryns, J. Hanes, D. Akin, J. B. Hall, N. Gharkholo, R. J. Mumper, *Nanomedicine* **2013**, *8*, 299.

[15] R. M. Crist, J. H. Grossman, A. K. Patri, S. T. Stern, M. A. Dobrovolskaia, P. P. Adiseshaiah, J. D. Clogston, S. E. McNeil, *Integr. Biol.* **2013**, *5*, 66.

[16] A. Wei, J. G. Mehtala, A. K. Patri, *J. Controlled Release* **2012**, *164*, 236.

www.MaterialsViews.com

ADVANCED
FUNCTIONAL
MATERIALS
www.afm-journal.de

FULL PAPER

[17] W. C. Zamboni, V. Torchilin, A. K. Patri, J. Hrkach, S. Stern, R. Lee, A. Nel, N. J. Panaro, P. Grodzinski, *Clin. Cancer Res.* **2012**, *18*, 3229.

[18] C. Kut, Y. Zhang, M. Hedayati, H. Zhou, C. Cornejo, J. Mihalic, C. Gruettner, A. Geyh, C. Brayton, T. L. DeWeese, R. Ivkov, *Nanomedicine* **2012**, *7*, 1697.

[19] M. W. Dewhirst, B. L. Viglianti, M. Lora-Michiels, M. Hanson, P. J. Hoopes, *Int. J. Hyperthermia* **2003**, *19*, 267.

[20] J. L. R. Roti, R. K. Pandita, J. D. Mueller, P. Novak, E. G. Moros, A. Laszlo, *Int. J. Hyperthermia* **2010**, *26*, 67.

[21] P. M. Krawczyk, B. Eppink, J. Essers, J. Stap, H. Rodermond, H. Odijk, A. Zelensky, C. van Bree, L. J. Stalpers, M. R. Buist, T. Soullie, J. Rens, H. J. M. Verhagen, M. J. O'Connor, N. A. P. Franken, T. L. M. ten Hagen, R. Kanaar, J. A. Aten, *Proc. Natl. Acad. Sci.* **2011**, *108*, 9851.

[22] J. L. Roti Roti, *Int. J. Hyperthermia* **2008**, *24*, 3.

[23] C. L. Dennis, R. Ivkov, *Int. J. Hyperthermia* **2013**, *29*, 715.

[24] C. L. Dennis, A. J. Jackson, J. A. Borchers, P. J. Hoopes, R. Strawbridge, A. R. Foreman, J. van Lierop, C. Grüttner, R. Ivkov, *Nanotechnology* **2009**, *20*, 395103.

[25] R. K. Gilchrist, R. Medal, W. D. Shorey, R. C. Hanselman, J. C. Parrott, C. B. Taylor, *Ann. Surg.* **1957**, *146*, 596.

[26] W. J. Atkinson, I. A. Brezovich, D. P. Chakraborty, *IEEE Trans. Biomed. Eng.* **1984**, *31*, 70.

[27] C. L. Dennis, A. J. Jackson, J. A. Borchers, R. Ivkov, A. R. Foreman, J. W. Lau, E. Goernitz, C. Gruettner, *J. Appl. Phys.* **2008**, *103*, 07A319.

[28] C. L. Dennis, A. J. Jackson, J. A. Borchers, R. Ivkov, A. R. Foreman, P. J. Hoopes, R. Strawbridge, Z. Pierce, E. Goernitz, J. W. Lau, C. Gruettner, *J. Phys. D: Appl. Phys.* **2008**, *41*, 134020.

[29] R. E. Rosensweig, *J. Magn. Magn. Mater.* **2002**, *252*, 370.

[30] D. E. Bordelon, C. Cornejo, C. Gruttner, F. Westphal, T. L. DeWeese, R. Ivkov, *J. Appl. Phys.* **2011**, *109*, 124904.

[31] L. C. Branquinho, M. S. Carriao, A. S. Costa, N. Zufelato, M. H. Sousa, R. Miotto, R. Ivkov, A. F. Bakuzis, *Sci. Rep.* **2013**, *3*, 28.

[32] B. E. Kashevsky, S. B. Kashevsky, I. V. Prokhorov, *Particuology* **2009**, *7*, 451.

[33] N. A. Usov, B. Ya Liubimov, *J. Appl. Phys.* **2012**, *112*, 023901.

[34] D. E. Bordelon, R. C. Goldstein, V. S. Nemkov, A. Kumar, J. K. Jackowski, T. L. DeWeese, R. Ivkov, *IEEE Trans. Magn.* **2012**, *48*, 47.

[35] The particles come from lot #0400784-W2.

[36] We identify certain commercial equipment, instruments, or materials in this article to specify adequately the experimental procedure. In no case does such identification imply recommendation or endorsement by the National Institute of Standards and Technology, nor does it imply that the materials or equipment identified are necessarily the best available for the purpose.

[37] C. Gruettner, K. Mueller, J. Teller, F. Westphal, A. Foreman, R. Ivkov, *J. Magn. Magn. Mater.* **2007**, *311*, 181.

[38] The particles come from lot #5120945.

[39] M. Hedayati, A. Attaluri, D. Bordelon, R. Goh, M. Armour, H. Zhou, C. Cornejo, M. Wabler, Y. Zhang, T. L. DeWeese, R. Ivkov, *Proc. SPIE* **2013**, *8584*, 858404.

[40] The particles come from lot #1151079.

[41] C. Grüttner, J. Teller, W. Schütt, F. Westphal, C. Schümichen, B. R. Paulke, in *Scientific and Clinical Application of Magnetic Carriers*, (Eds: U. O. Hafeli, W. Schütt, J. Teller, M. Zborowski), Plenum, New York **1997**, pp 53–68.

[42] S. Taketomi, R. D. Shull, *J. Appl. Phys.* **2002**, *91*, 8546.

[43] P. Poddar, M. B. Morales, N. A. Frey, S. A. Morrison, E. E. Carpenter, H. Srikanth, *J. Appl. Phys.* **2008**, *104*, 063901.

[44] A. Aharoni, E. H. Frei, S. Shtrikman, D. Treves, *Bull. Res. Counc. Isr.* **1957**, *6A*, 215.

[45] S. Chikazumi, *Physics of Ferromagnetism*, 2nd ed., Oxford University Press, New York **1997**, p 27.

[46] J. Carrey, B. Mehdaoui, M. Respaud, *J. Appl. Phys.* **2011**, *109*, 083921.

[47] S. R. Kline, *J. Appl. Crystallogr.* **2006**, *39*, 895.

[48] K. Krycka, W. C. Chen, J. Borchers, B. Maranville, S. Watson, *J. Appl. Crystallogr.* **2012**, *45*, 546.

[49] K. Krycka, J. Borchers, Y. Ijiri, R. Booth, S. Majetich, *J. Appl. Crystallogr.* **2012**, *45*, 554.

[50] K. L. Krycka, R. A. Booth, C. R. Hogg, Y. Ijiri, J. A. Borchers, W. C. Chen, S. M. Watson, M. Laver, T. R. Gentile, L. R. Dedon, S. Harris, J. J. Rhyne, S. A. Majetich, *Phys. Rev. Lett.* **2010**, *104*, 207203.

[51] J. L. Dormann, D. Fiorani, E. Tronc, in *Advances in Chemical Physics*, (Eds: I. Prigogine, S. A. Rice) Wiley, New York **1997**, pp 283–494, Vol. XCVIII.

[52] M. J. Donahue, D. G. Porter, OOMMF User's Guide, Version 1.0, Interagency Report NISTIR 6376, National Institute of Standards and Technology, Gaithersburg, MD, http://math.nist.gov/oommf/ (accessed: September 1999).

[53] A. Attaluri, C. Nusbaum, M. Wabler, R. Ivkov, *J. Nanotechnol. Eng. Med.* **2013**, *4*, 011006.